Supplementary Information for
Bilateral Geiger mode avalanche in InSe Schottky photodiodes

Dongyang Zhao[1,2#], Yan Chen[2,3#*], Tao Hu[1,2], Hechun Cao[1,2], Xuefeng Zhao[1], Yu Jia[1], Xudong Wang[2*], Hong Shen[2], Jing Yang[1], Yuanyuan Zhang[1], Xiaodong Tang[1], Wei Bai[1*], Jianlu Wang[2,3,4], and Junhao Chu[2,3]

[1]Key Laboratory of Polar Materials and Devices (MOE) and Department of Electronics, East China Normal University, Shanghai 200241, P. R. China

[2]State Key Laboratory of Infrared Physics, Shanghai Institute of Technical Physics, Chinese Academy of Sciences, No.500 Yutian Road, Shanghai 200083, P. R. China.

[3]Shanghai Frontier Base of Intelligent Optoelectronics and Perception, Institute of Optoelectronics, Fudan University, 200433 Shanghai, P. R. China

[4]Frontier Institute of Chip and System, Fudan University, Shanghai 200433, P. R. China

E-mail: yanchen_@fudan.edu.cn, wxd0130@mail.sitp.ac.cn, and wbai@ee.ecnu.edu.cn

Table of contents

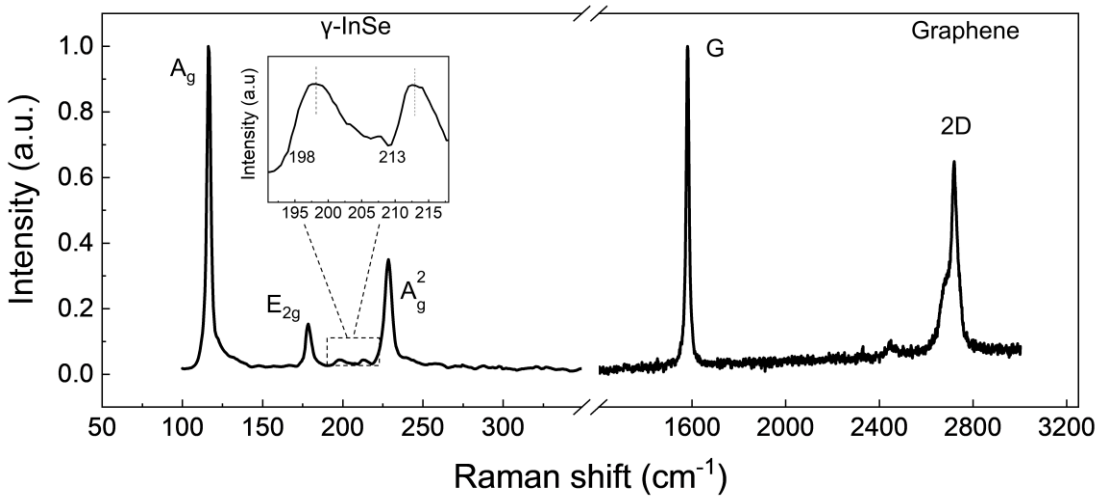

Supplementary Fig. S1| Raman spectra of the overlapped InSe/Graphene area. The Raman spectrum of InSe displays three main peaks at 114 cm^{-1}, 178 cm^{-1}, and 227 cm^{-1}, corresponding to A_1, E, and A_1 modes, respectively. Note that there are two weak peaks of the InSe nanosheet (black line in the inset), located at 198 and 213 cm^{-1} indicating that the InSe we used is γ-InSe. The Raman spectrum of Graphene displays two peaks at 1581 cm^{-1}, and 2720 cm^{-1}, corresponding to G and 2D modes.

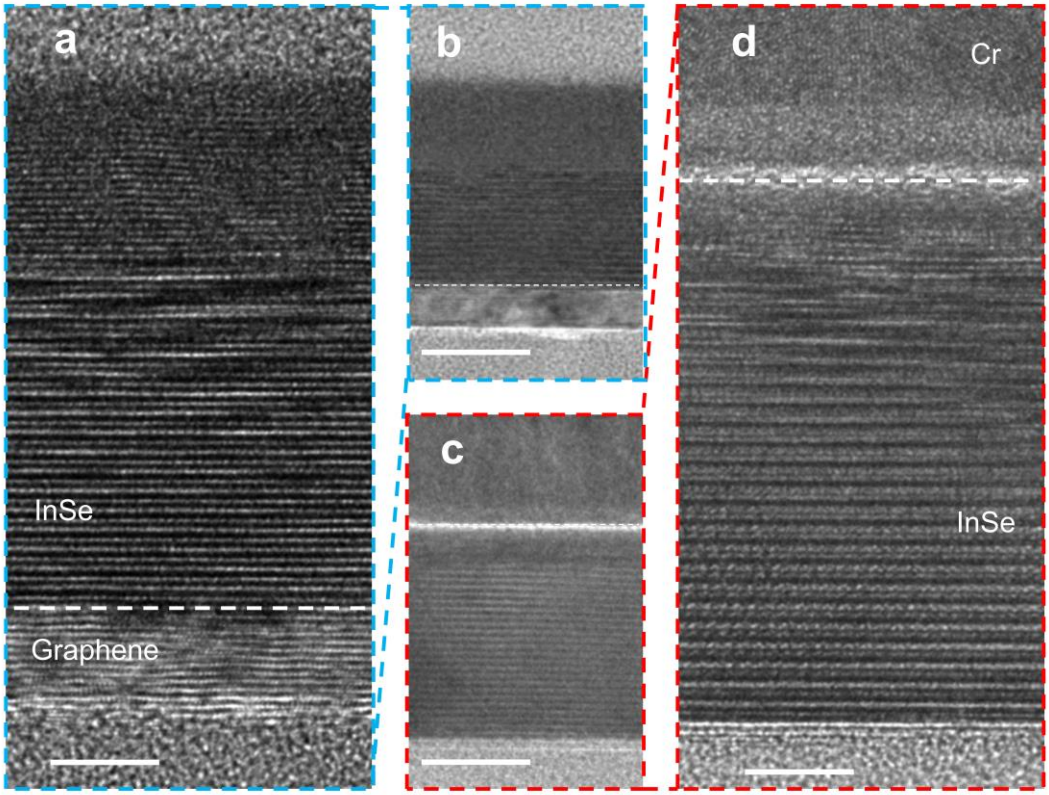

Supplementary Fig. S2| Interface characteristics of the InSe/Graphene and InSe/Cr contact. **a, b,** Low magnified cross-sectional HRTEM image of InSe/Graphene interface. **c, d,** Low magnified cross-sectional TEM image of InSe/Cr interface.

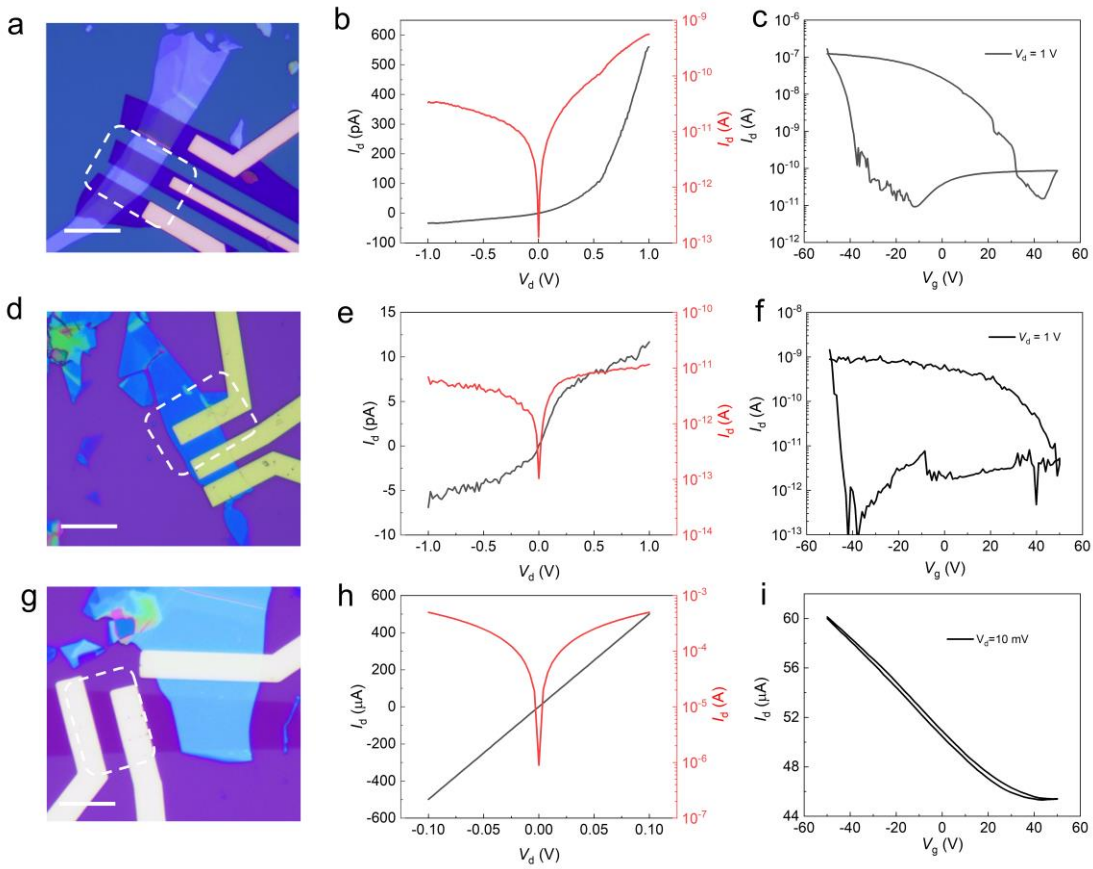

Supplementary Fig. S3| Electrical characterization of InSe and Graphene. a, Optical image of the InSe with symmetrical Graphene electrodes. **b,** *I-V* curve of InSe with Graphene electrodes. **c,** Transfer characteristic curves of InSe with Graphene electrodes at V_d = 1 V, showing p-type conduction property. **d,** Optical image of the InSe with symmetrical Cr electrodes. **e,** *I-V* curve of InSe with Cr electrodes. **f,** Transfer characteristic curves of InSe with Cr electrodes at V_d = 1 V, showing p-type conduction behavior. **g,** The optical image of the Graphene FET. **h,** *I-V* curve of Graphene FET. **i,** Transfer characteristic curve of Graphene FET.

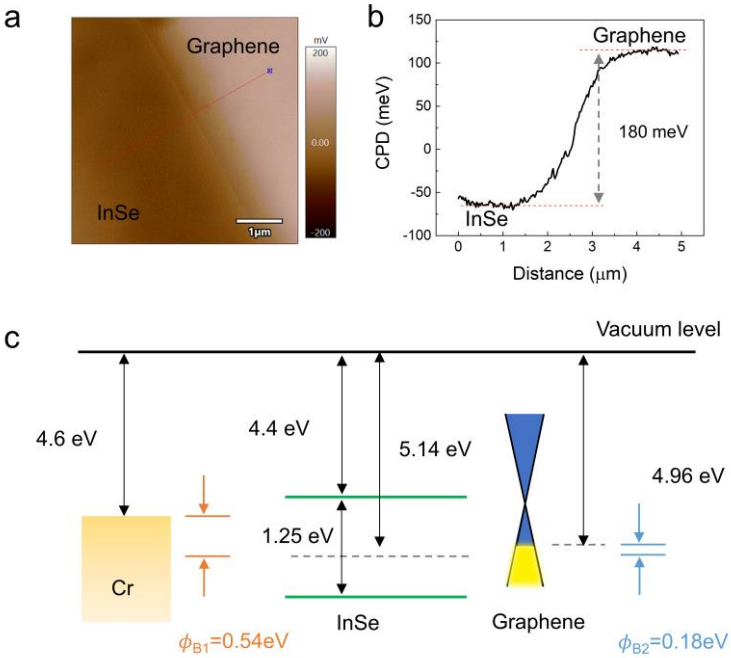

Supplementary Fig. S4| Energy band diagrams of Cr, InSe, and Graphene. a, Contact potential difference between InSe and Graphene flakes. **b,** Extracted contact potential difference between Graphene and InSe flakes from Figure a. **c**, Energy band diagrams of Cr, InSe, and Graphene.

The fermi-level difference between Graphene and InSe is determined by the difference between the two surface potentials ($\Delta E_F = E_F$(Graphene) − E_F(InSe) = eV_{CPD}(Graphene) − eV_{CPD}(InSe), where e is the charge of an electron and V_{CPD} represents local surface potential). The Fermi level difference between InSe and Graphene was 180 meV. Since the work function of Cr and Graphene is 4.6 eV and 4.96 eV, respectively.[1] We give the work function of InSe and calculate the Schottky barrier between the Cr and InSe. The work function of InSe is 5.14 eV showing p-type, which is consistent with the transfer characteristic curves in Fig. S3. The Schottky barrier between Cr and InSe is 0.54 eV, larger than that between Graphene and InSe. Therefore, two asymmetric Schottky contacts were formed in our device. Electrical test results (Fig. 2d and Fig. S5) suggest that the InSe Schottky diode can be fabricated successfully by using Cr and Graphene electrodes.

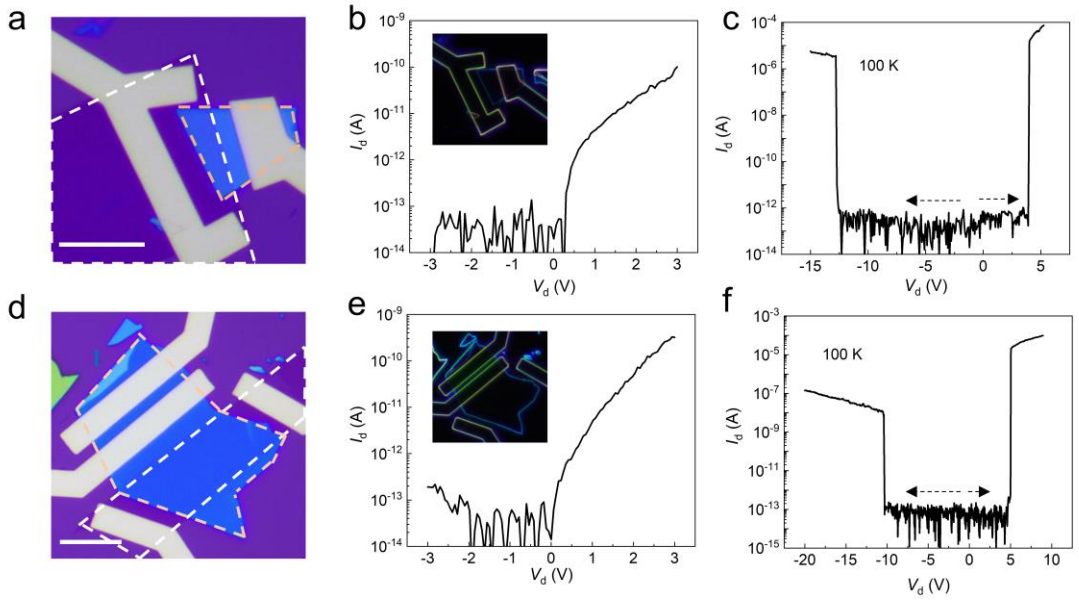

Supplementary Fig. S5| The *I-V* characteristic curves of the other two Cr/InSe/Graphene Schottky diode devices. a, d, Optical picture of the devices with asymmetric Cr and Graphene electrodes. The white dotted boxes represent Graphene and the orange dotted boxes represent InSe. The scale bar is 10 μm. **b, e,** The *I-V* curves of the devices were measured at room temperature within a low bias range, which shows obvious rectification behavior. Besides, it exhibits an ultralow dark current of about 10^{-13} A at V_d = -3 V. The insert is the darkfield images of the devices indicating a very clean interface between the transferred InSe and Graphene. **c, f,** The *I-V* curves of the devices were measured at 100 K, showing a steep avalanche breakdown. The voltage firstly swept from 0 V to -20 V and then from 0 V to 5 V.

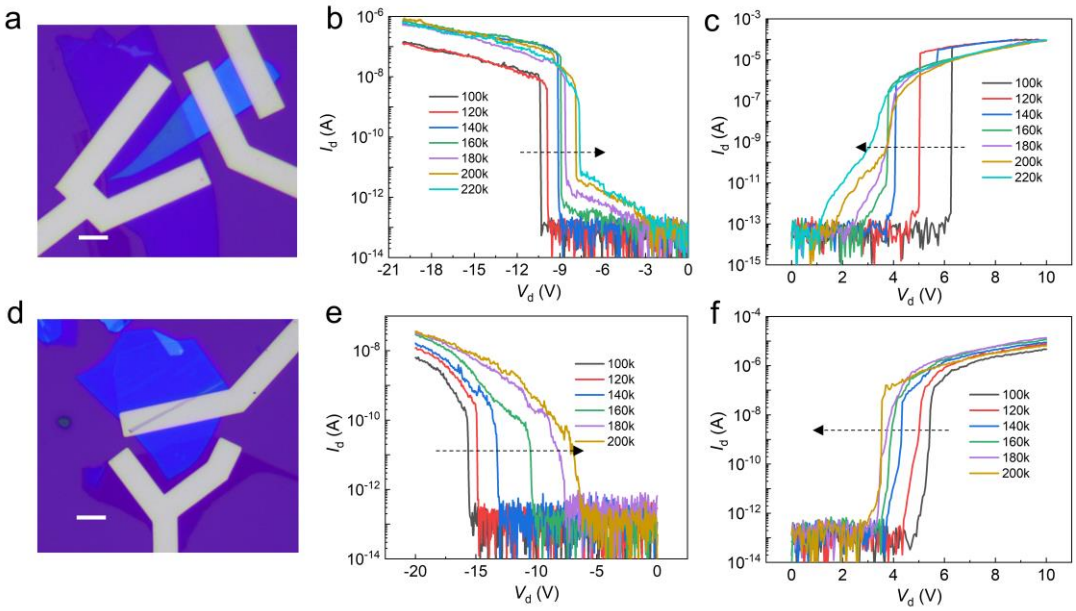

Supplementary Fig. S6| The temperature-dependent variations of avalanche breakdown voltage. a, d, Optical image of the Graphene/InSe/Cr devices. **b, e**, Avalanche breakdown characteristics of devices when they were reverse-biased. **c, f**, Avalanche breakdown characteristics of devices when they were forward-biased.

All devices show the same negative temperature coefficient of breakdown voltage consistent with the reported phenomenon in the main text. This demonstrates that the temperature-dependent variations of breakdown voltage in the main text are reproducible.

Supplementary Note1. Determination of α from the multiplication factor (M)

When avalanche multiplication occurs in a junction denoted as $0 \leq x \leq L$, then the relationship between the multiplication factor M and the impact ionization rate α is given as the following equation[2]:

$$1 - \frac{1}{M} = \int_0^L \alpha_n(E) \exp\left\{-\int_0^x \alpha_n(E) - \alpha_p(E) dx'\right\} dx \quad \text{S1}$$

It is assumed that the impact ionization rates of electrons and holes are comparable. And this assumption does not influence the final result critically. With this assumption, the relationship between the multiplication factor M and the impact ionization rate α is given by the equation

$$1 - \frac{1}{M} = \int_0^L \alpha(E) dx \quad \text{S2}$$

Note that E can be a function of x. In addition, it is assumed that the electric field in the channel does not depend on the position x. Then, the x-dependence of α disappears, and we obtain the equation

$$1 - \frac{1}{M} = L\alpha \quad \text{S3}$$

which is the relation we used to calculate α from M.

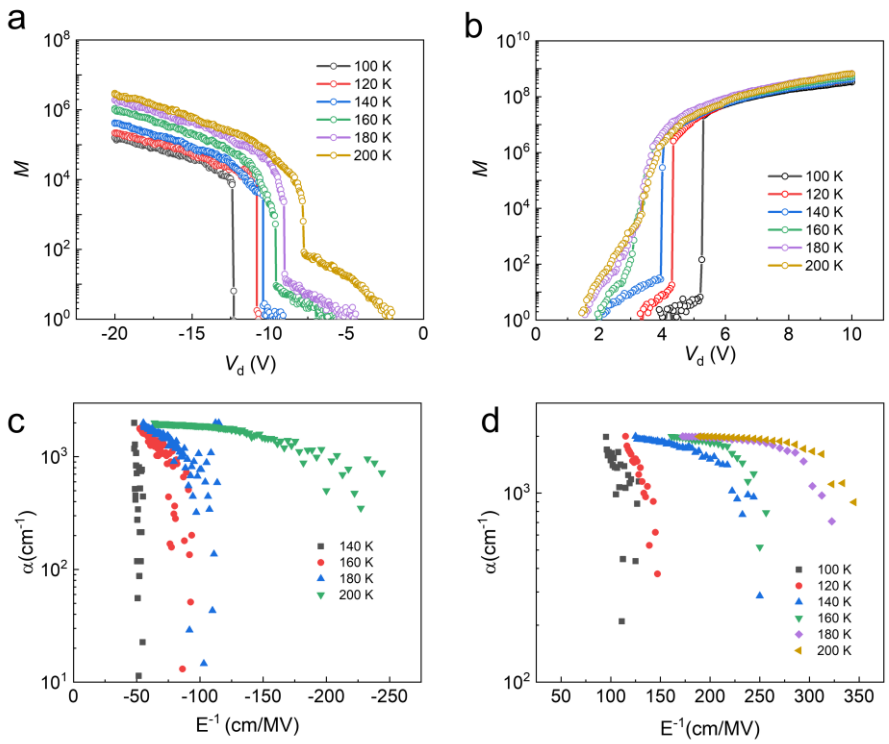

Supplementary Fig. S7| Temperature-dependent *M* and *α* at both reverse and forward bias. a, b, Calculated *M* under different temperatures as a function of bias voltage from Fig. 3a at reverse and forward bias. **c, d,** Calculated ionization impact rates at different temperatures as a function of the inverse field under reverse and forward bias.

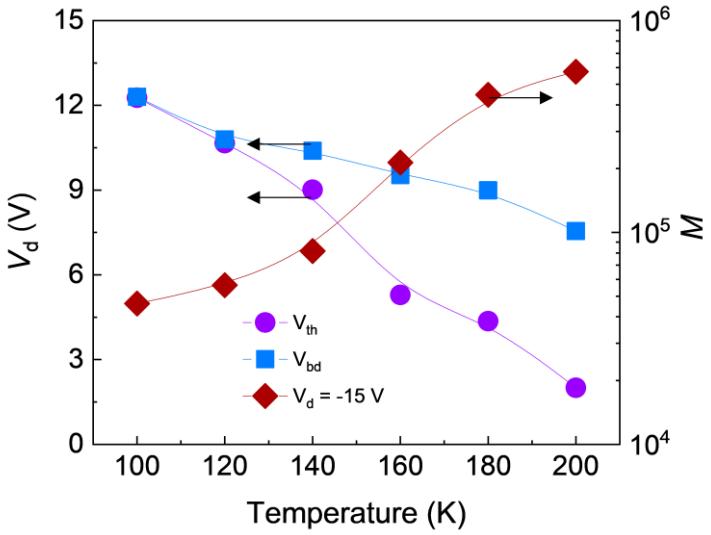

Supplementary Fig. S8| **The dependence of the V_{th}, V_{bd}, and M on the temperature at the reverse bias case extracted from Supplementary Fig. S7a.**

It is obvious that the reverse bias operation of the device shows the same tendency for the dependence of V_{th}, V_{bd}, and M on temperature as that of forward operation.

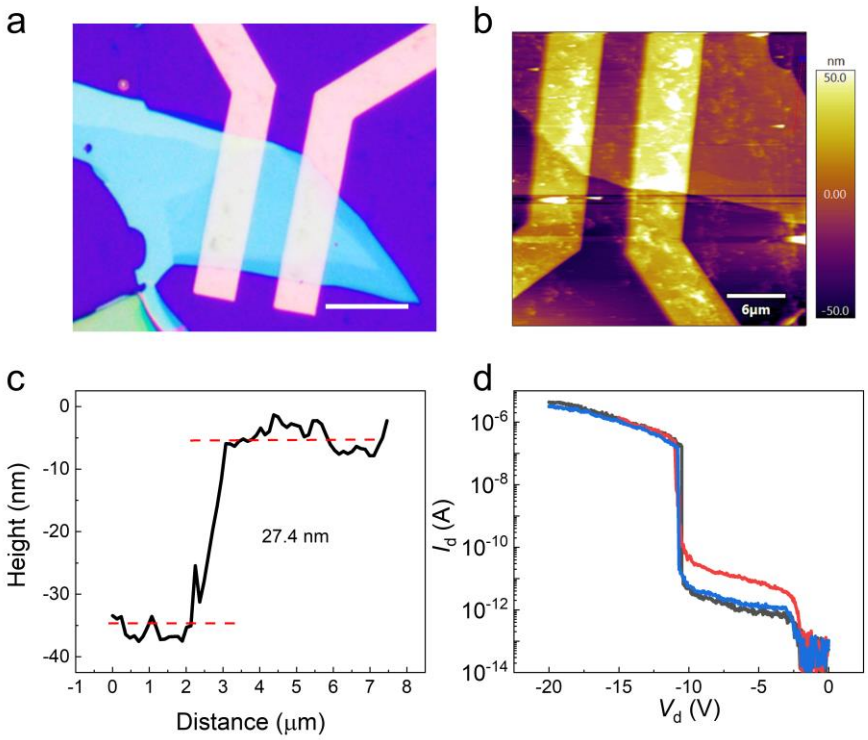

Supplementary Fig. S9| The breakdown voltage of the Cr/InSe/Cr device. a, The optical microscope images of the five Cr/InSe/Cr devices. **b,** AFM images of the five devices with a scanning range of 30 μm × 30 μm. **c,** Height profiles extracted from AFM results, showing the thickness is 27.4 nm. **d,** The *I-V* curves of the corresponding devices showing avalanche breakdown character with a breakdown voltage around 10.6 V.

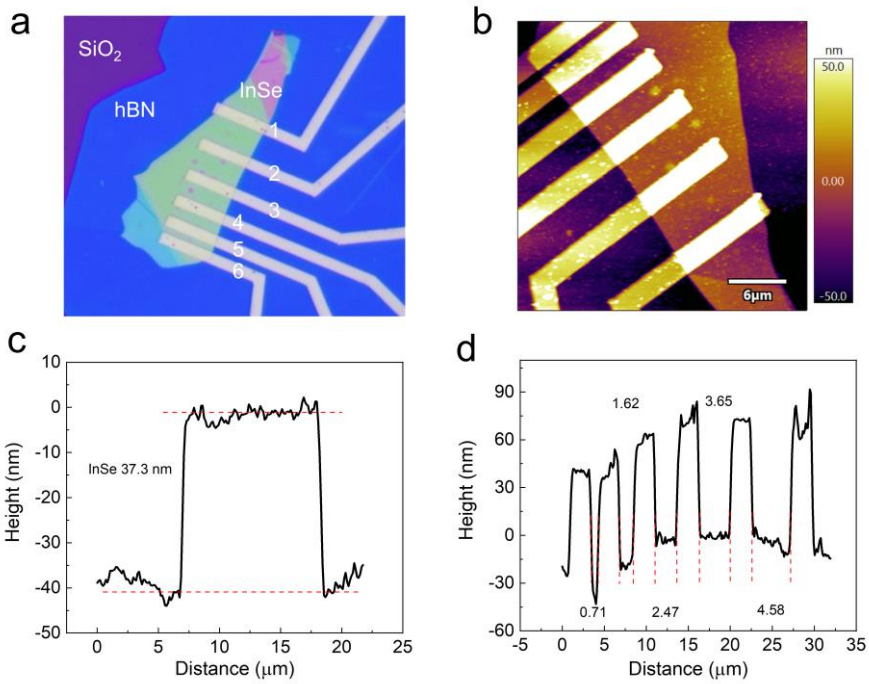

Supplementary Fig. S10| AFM characterization of the Cr/InSe/Cr APD fabricated on hBN. a, Optical image of C/InSe/Cr APD on hBN. The channel width of each device is guaranteed to be around 10 μm. **b,** An AFM image of the device shows the thickness of InSe and the channel length of adjacent electrodes. **c,** Height profiles of InSe extracted from AFM results. The thickness of the InSe is about 37.3 nm. **d,** Channel length profiles extracted from AFM results. The length of each channel is 0.71, 1.62, 2.47, 3.65, and 4.58 μm in ascending order.

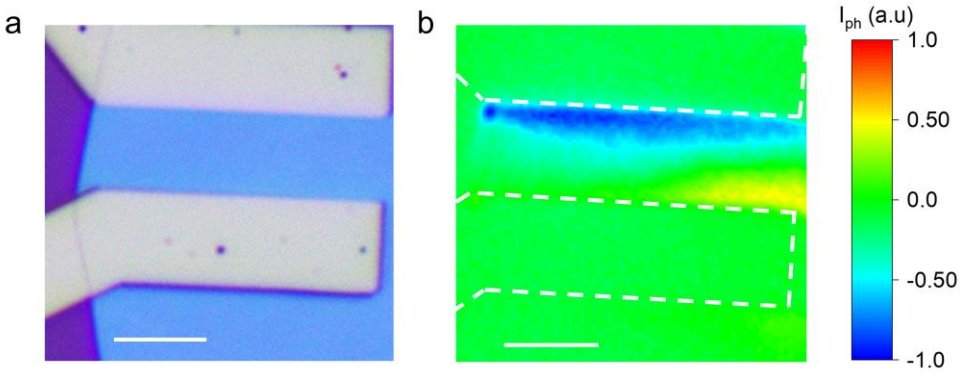

Supplementary Fig. S11| Scanning photocurrent mapping (SPCM) experiments on InSe SJ device. a, Optical image of the Cr/InSe/Cr SJ device. The scale bar is 5 μm. **b,** Corresponding SPCM images at a reverse bias of 1.4 V showing the depletion region width is around 1.5 μm. The scale bar is 5 μm.

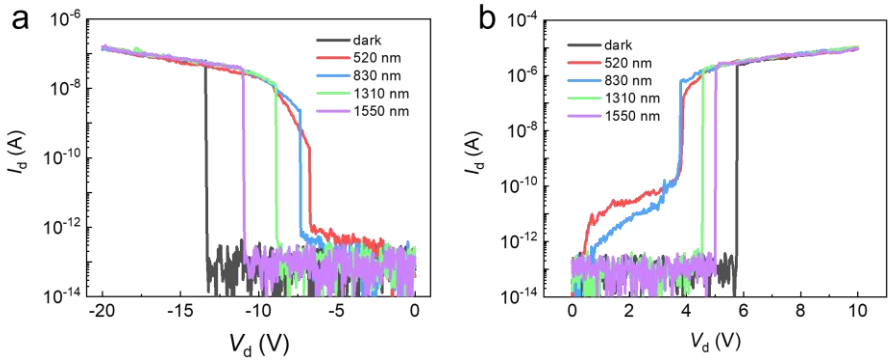

Supplementary Fig. S12| Optical response characteristics of the GISC-SJ SJ APD at reverse and forward bias voltages at 100 K. a, The *I–V* curves of the device in a dark state and illumination under different wavelengths of light under reverse bias. **b,** The *I–V* curves of the device in a dark state and illumination under different wavelengths of light under forward bias.

The GISC-SJ APDs show an obvious response to light illumination at both forward and reverse bias operations. This confirms that the current breakdown is indeed from the avalanche process at both operation modes since light illumination will not affect the Zener breakdown. Besides, it is worth noting that the device could respond to 1310 and 1550 nm beyond the cut-off wavelength of InSe. This phenomenon should be attributed to the internal photoelectron emission (IPE) effect.[3,4] For light beyond the cut-off wavelength of InSe, if the energy of hot electrons emitted from Cr (Graphene) is higher than the Schottky barrier at the interface of the Cr/InSe and Graphene/InSe junction ($0.5\ h\nu > \phi_{SBH}$), photoexcited hot electrons directly transport over the barrier and trigger impact ionization.

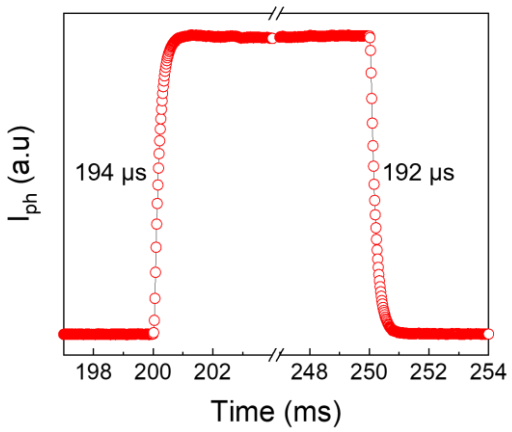

Supplementary Fig. S13| Photoresponse performance of the GISC-SJ device at room temperature.

Since the spot size of the laser is concentrated and is smaller than the effective detection area of the APD, the actual lowest optical power on our device is 5.7 pW. Based on the response time ~ 190 μs, the corresponding photodetection limit is about 2900 photons (5.7 pW× 194 $\mu s/hv_{520}$).

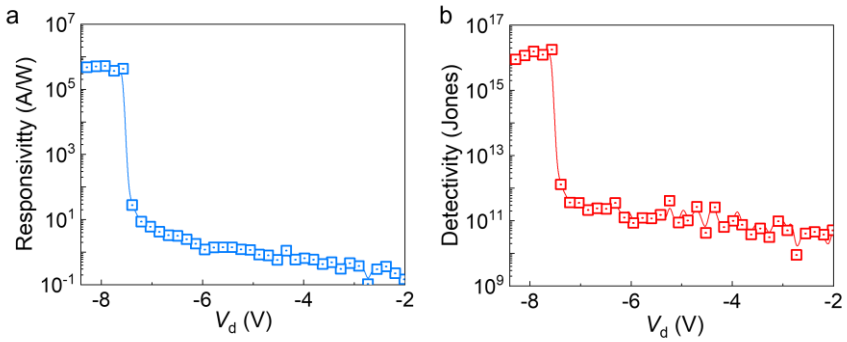

Supplementary Fig. S14| Responsivity and Detectivity as a function of reverse bias. a, Calculated responsivity of the APD as a function of reverse bias. **b,** Calculated detectivity of the APD as a function of reverse bias.

The responsivity $R = I_{ph}/P_{eff}$ indicates how much photocurrent can be produced by unit incident power on the photodetector, while the detectivity is given by $D^* = RA^{1/2}(2eI_{dark})^{-1/2}$. Here R and D^* are given at P_{eff} =5.7 pW.

Supplementary Table 1. Summary of the *M* and breakdown voltage reported in this work and previous literatures with different types of material.

Material	Temperature (K)	V_d (V)	I_{dark} (A)	*M*	Ref.
Si	300	40	-	6×10^{6}	5
Si/Ge	300	10.3	1×10^{-10}	1.2×10^{2}	6
InGaAs/InP	225	61.0	1×10^{-11}	1.0×10^{5}	7
InAlAsSb	300	19.6	1×10^{-7}	7.0×10^{3}	8
InAlAsSb/GaSb	300	45.0	1×10^{-6}	1.5×10^{2}	9
WSe_2/MoS_2	300	30	5×10^{-10}	1.0×10^{3}	10
WSe_2	300	3	1×10^{-11}	4.7×10^{2}	11
WSe_2	300	24	1×10^{-14}	5.0×10^{5}	12
MoS_2	100	20	1×10^{-12}	1.2×10^{3}	13
InSe	160	5.1	1×10^{-12}	3×10^{5}	14
InSe	100	3.9	1×10^{-13}	2.3×10^{7}	This work

Here, the M value of 2.3×10^{7} and the corresponding V_d of 3.9 V are extracted from Fig. S5c. The highest M value of 6.3×10^{7} is extracted from Fig. S5f.

Supplementary Table 2. Comparison of E_{CR} for different types of materials.

Material	Indirect bandgap (eV)	E_{CR} (kV/cm)	Ref.
Ge	0.66	100	15
Si	1.12	300	15
GaP	2.26	1000	15
SiC(3C, β)	2.36	1300	15
SiC(6H, α)	2.96	2400	15
SiC(4H, α)	3.25	3180	15
MoS_2	1.2	960	16
WSe_2	1.0	75	17
BP	0.3	55	18
InSe	1.25	11.5	This work

Supplementary Table 3. Comparison of responsivity and detectivity of the InSe Schottky junctions APD with reported PV, PG, and APD photodetectors based on 2D materials.

Device type	Material	Wavelength (nm)	Responsivity (A/W)	Detectivity (Jones)	Ref.
PV	InSe	785	7.5×10^{0}	4.6×10^{13}	19
	InSe/Graphene	400	3.0×10^{-1}	1.3×10^{13}	20
	InSe/AsP	520	1.0×10^{0}	1.0×10^{12}	21
	InSe/GaTe	520	3.0×10^{1}	2.0×10^{13}	22
	InSe/GaSe	410	3.5×10^{2}	2.2×10^{13}	23
PG	InSe	532	1.4×10^{4}	1.6×10^{13}	24
	InSe/WSe_2	532	1.0×10^{4}	1.3×10^{13}	25
	InSe/ReS_2	365	1.9×10^{3}	6.5×10^{13}	26
APD	InSe/Ti_2CT_x	405	1.0×10^{5}	7.3×10^{12}	27
	WSe_2/MoS_2	532	1.4×10^{2}	1.3×10^{12}	28
	Bi_2O_2Se	516	3.0×10^{3}	4.6×10^{14}	29
	Cr/InSe/Graphene	520	4.5×10^{5}	1.8×10^{16}	This work

PV is short for photovoltaic and PG is short for photogating.

References

1. Chen, Y*, et al.* Unipolar barrier photodetectors based on van der Waals heterostructures. *Nat. Electron*. **4**, 357-363(2021).
2. Kim, J*, et al.* Channel-Length-Modulated Avalanche Multiplication in Ambipolar WSe2 Field-Effect Transistors. *ACS Nano*. **16**, 5376-5383(2022).
3. Li, Z*, et al.* Telecom-Band Waveguide-Integrated MoS2 Photodetector Assisted by Hot Electrons. *ACS Photonics*. **9**, 282-289(2022).
4. Peng, L*, et al.* Macroscopic assembled graphene nanofilms based room temperature ultrafast mid-infrared photodetectors. *InfoMat*. **4**, e12309(2022).
5. Hamamatsu S16835 series. https://www.hamamatsu.com.cn/cn/zh-cn/product/optical-sensors/mppc/spad/S16835-050DG.html
6. Na, NL*, et al.* Room temperature operation of germanium-silicon single-photon avalanche diode. *Nature.***627**, 295-300(2024).
7. Signorelli, F*, et al.* Low-Noise InGaAs/InP Single-Photon Avalanche Diodes for Fiber-Based and Free-Space Applications. *IEEE J. Sel. Top. Quantum. Electron*. **28**, 1-10(2022).
8. Chen, D*, et al.* Photon-trapping-enhanced avalanche photodiodes for mid-infrared applications. *Nat. Photon*. **7**, 594-600(2023).
9. Jones, AH*, et al.* Low-noise high-temperature AlInAsSb/GaSb avalanche photodiodes for 2-μm applications. *Nat. Photon*. **14**, 559-563(2020).
10. Son, B*, et al.* Efficient Avalanche Photodiodes with a WSe_2/MoS_2 Heterostructure via Two-Photon Absorption. *Nano Lett*. **22**, 9616-9522(2022).
11. Wang, H*, et al.* Room-temperature low-threshold avalanche effect in stepwise van-der-Waals homojunction photodiodes. *Nat. Commun*. **15**, 3639(2024).
12. Li, X*, et al.* Achieving a Noise Limit with a Few-layer WSe_2 Avalanche Photodetector at Room Temperature. *Nano Lett.* **24**,13255–13262(2024).
13. Xia, H*, et al.* Pristine PN junction toward atomic layer devices. *Light. Sci. Appl*. **11**, 170(2022).
14. Zhang, Z*, et al.* Approaching intrinsic threshold breakdown voltage and ultra-high gain in graphite/InSe Schottky photodetector. *Adv Mater*, e2206196(2022).
15. Hudgins, JL*, et al.* An assessment of wide bandgap semiconductors for power devices. *IEEE Trans. Power Electron*. **18**, 907-914(2003).
16. Pak, J*, et al.* Two-Dimensional Thickness-Dependent Avalanche Breakdown Phenomena in MoS_2 Field-Effect Transistors under High Electric Fields. *ACS Nano*. **12**, 7109-7116(2018).
17. Choi, H*, et al.* A steep switching WSe_2 impact ionization field-effect transistor. *Nat. Commun*. **13**, 6076(2022).
18. Ahmed, F*, et al.* Impact ionization by hot carriers in a black phosphorus field effect transistor. *Nat. Commun*. **9**, 3414(2018).
19. Wang, X*, et al.* Strong Anisotropy of Multilayer γ-InSe-Enabled Polarization Division Multiplexing Photodetection. *Adv. Photon. Res*. **3**, 2200119(2022).

20. Dai, M*, et al.* Ultrafast and Sensitive Self-Powered Photodetector Featuring Self-Limited Depletion Region and Fully Depleted Channel with van der Waals Contacts. *ACS Nano*. **14**, 9098-9106(2020).
21. Wu, F*, et al.* AsP/InSe Van der Waals Tunneling Heterojunctions with Ultrahigh Reverse Rectification Ratio and High Photosensitivity. *Adv. Funt. Mater*. **29**, 1900314(2019).
22. Qi, T*, et al.* Interlayer Transition in a vdW Heterostructure toward Ultrahigh Detectivity Shortwave Infrared Photodetectors. *Adv. Funct. Mater*. **30**, 1905687(2019).
23. Chen, X*, et al.* Van der Waals Nonlinear Photodetector with Quadratic Photoresponse. *Nano Lett*. **23**, 1023-1029(2023).
24. Liu, L*, et al.* Ferroelectric-Gated InSe Photodetectors with High On/Off Ratios and Photoresponsivity. *Nano Lett*. **20**, 6666-6673(2020).
25. Lei, T*, et al.* Ambipolar Photoresponsivity in an Ultrasensitive Photodetector Based on a WSe_2/InSe Heterostructure by a Photogating Effect. *ACS Appl. Mater. Interfaces*. **13**, 50213-50219(2021).
26. Ma, H*, et al.* Ultrasensitive and Broad-Spectrum Photodetectors Based on InSe/ReS_2 Heterostructure. *Adv. Opt. Mater*. **10**, 2101772(2021).
27. Yang, Y*, et al.* Plasmonic Transition Metal Carbide Electrodes for High-Performance InSe Photodetectors. *ACS Nano*. **13**, 8804-8810(2019).
28. Meng, L*, et al.* Low-voltage and high-gain WSe_2 avalanche phototransistor with an out-of-plane WSe_2/WS_2 heterojunction. *Nano Res*. **16**, 3422-3428(2022).
29. Sangwan, VK*, et al.* Intrinsic carrier multiplication in layered Bi2O2Se avalanche photodiodes with gain bandwidth product exceeding 1 GHz. *Nano Res*. **14**, 1961-1966(2020).